Journal Pre-proofs

Co-catalytic effect of WS_2 on the copper slag mediated peroxodisulfate activation for the simultaneous elimination of typical flotation reagent benzotriazole and Cr(VI)

Bo Ma, Jun Yao, Tatjana Šolević Knudsen, Zhihui Chen, Wancheng Pang, Bang Liu, Ying Cao, Xiaozhe Zhu, Chenchen Zhao

PII: S1385-8947(22)04367-4
DOI: https://doi.org/10.1016/j.cej.2022.138888
Reference: CEJ 138888

To appear in: *Chemical Engineering Journal*

Received Date: 17 May 2022
Revised Date: 9 August 2022
Accepted Date: 25 August 2022

Please cite this article as: B. Ma, J. Yao, T. Šolević Knudsen, Z. Chen, W. Pang, B. Liu, Y. Cao, X. Zhu, C. Zhao, Co-catalytic effect of WS_2 on the copper slag mediated peroxodisulfate activation for the simultaneous elimination of typical flotation reagent benzotriazole and Cr(VI), *Chemical Engineering Journal* (2022), doi: https://doi.org/10.1016/j.cej.2022.138888

Co-catalytic effect of WS_2 on the copper slag mediated peroxodisulfate activation for the simultaneous elimination of typical flotation reagent benzotriazole and Cr(VI)

Bo Ma,[a] Jun Yao,[a,*] Tatjana Šolević Knudsen,[b] Zhihui Chen,[a] Wancheng Pang,[a] Bang Liu,[a] Ying Cao,[a] Xiaozhe Zhu,[a] Chenchen Zhao[a]

[a]School of Water Resources and Environment, Research Center of Environmental Science and Engineering, China University of Geosciences (Beijing), Beijing 100083, China

[b]University of Belgrade, Institute of Chemistry, Technology and Metallurgy, Department of Chemistry, Njegoševa 12, 11000 Belgrade, Serbia

*Corresponding author at: School of Water Resources and Environment, China University of Geosciences (Beijing), 29 Xueyuan Road, Haidian District, Beijing, 100083, China. E-mail: yaojun@cugb.edu.cn (Jun Yao)

ABSTRACT

In this study, efficient simultaneous elimination of typical mine pollutants benzotriazole (BTA) and Cr(VI) was achieved by using a copper slag (CS) activated peroxodisulfate (PDS) Fenton system, with WS_2 as a co-catalyst. The combined use of these two mine-sourced materials enables excellent pollution removal efficiency. CS can continuously release ferrous ions for the advanced oxidation processes (AOPs), while WS_2 as a co-catalyst has key roles in acceleration of the rate-limiting step of Fe^{3+}/Fe^{2+} conversion and prevention of Fe^{3+} precipitation. In this process, Fe^{3+}/Fe^{2+} conversion primarily occurs on the surface of WS_2, whereas PDS decomposition and BTA degradation are dominated by homogeneous Fenton reactions. Dissolved Fe^{2+} has a main role in the activation of PDS and generation of ROS. The contributions of free radicals, singlet oxygen and Fe(IV) in BTA degradation were carefully evaluated. Fe(IV) was identified as the major ROS responsible for degradation of BTA in the $CS/WS_2/PDS$ system. This was further confirmed by the Raman spectra and the detection of BTA degradation products formed by the transfer of oxygen atoms. Kinetics calculation showed that Fe(IV) was responsible for 63.4% of the degradation of BTA. More importantly, water matrix had a low impact on the degradation of BTA due to the high selectivity of Fe(IV). This study provides a new strategy for a cost-effective and efficient decontamination of the environment in mining areas.

Keywords: Copper Slag; Metal Sulfide; Iron Redox Cycle, Ferryl; Combined Pollution; Kinetics

1. Introduction

Long-term mining activities have caused serious pollution in the environment, which is the inevitable result of the economic development and social demand for mineral products. Mining pollution not only contains various metal(loid)s, but it also contains a large number of mineral organic flotation reagents [1, 2]. BTA, an emerging contaminant, is widely applied to extraction of minerals [3-5]. However, this compound is a proven endocrine disruptor which is also resistant to biodegradation [6]. Due to its high toxicity, carcinogenicity and teratogenicity Cr(VI) is one of the most toxic pollutants in the mine environment [7]. Cr(III) is thermodynamically the most stable oxidation state of this element, kinetically inert, and significantly less toxic [8]. Therefore, development of a highly efficient system that is able to degrade organic flotation reagents and simultaneously reduce Cr(VI) to Cr(III) is imperative.

Peroxydisulfate (PDS; $S_2O_8^{2-}$) based advanced oxidation processes (AOPs) have been widely employed for elimination of organic pollutants from wastewater [9, 10]. However, homogeneous AOPs usually suffer from some drawbacks that lower their efficiency and limit their application [11, 12]. In order to overcome the difficulties encountered in the application of homogeneous AOPs, various heterogeneous catalysts have been developed so far [13, 14]. However, most of them are limited to laboratory studies or small trials. Furthermore, most of them are unacceptable for large-scale pollution remediation due to the high cost and hidden danger of secondary pollution. In that respect, a more sensible option would be to use iron-bearing solid waste as a

heterogeneous Fenton catalyst. One of the potential candidates to be used for this purpose is CS, a by-product of the copper flotation and refining [15, 16].

Despite the widespread utilization of heterogeneous catalysts, the decomposition rate of PDS is still very low due to the inefficiency of Fe(III)/Fe(II) cycle. Many efforts have been made to improve the inefficient transformation of Fe(III) to Fe(II). Some of them involved addition of various organic ligands [17, 18], organic carboxylic acids [19-21] or polyphenols [22, 23]. In comparison with organic co-catalysts, inorganic co-catalysts are more stable, eco-friendly and sustainable. Recently, researchers have found that metal sulfides such as WS_2, MoS_2 and ZnS can be used as co-catalysts to promote the Fenton process by accelerating the rate-limiting step of Fe(III)/Fe(II) transformation [24-26]. Among these metal sulfides, WS_2 has attracted much attention due to its stronger redox capacity, stable physicochemical property and abundant resources [25, 27]. However, these studies were more focused on the homogeneous Fenton system [24, 25, 28]. In addition, these studies lack in-depth critical discussion on the generated ROS. Almost all of them revealed that free radicals were the primary ROS only by quenching experiment or electron paramagnetic resonance (EPR) analysis. Recent studies revealed that non-radical ROS such as singlet oxygen ($^1O_2$) or ferryl iron (Fe(IV)) generated from iron activated Fenton reactions at neutral pH were primary working ROS, responsible for the degradation of organic compounds [29-33]. However, the generation of non-radical ROS has never been evaluated in the WS_2 co-catalyzed systems. It has remained unclear so far whether Fe(IV) or singlet oxygen can be

produced in the CS/WS_2/PDS system.

The objectives of this study are to: (1) investigate the possibilities for application of copper slag in degradation of BTA and reduction of Cr(VI), (2) evaluate the co-catalytic behavior of WS_2 on the CS/PDS heterogeneous Fenton process, and (3) elucidate the main ROS in the CS/WS_2/PDS system by diverse methods such as quenching experiments, in situ Raman spectrum, EPR analysis and product identification by gas chromatography-mass spectrometry (GC-MS).

2. Materials and methods

2.1. Materials

All details about the chemicals used in this study are presented in the Supporting Information Text S1. CS was obtained from Sichuan Pengcheng Mining Co., Ltd. The CS was air-dried, then milled with an agate mortar and screened through a 100-mesh sieve.

2.2. Simultaneous oxidation of BTA and reduction of Cr(VI)

The simultaneous removal experiments of BTA and Cr(VI) were performed in 50 mL centrifuge tubes with 20 mg/L of BTA, 20 mg/L of Cr(VI) and 3 mM of PDS. The initial pH was adjusted to 3.0 ± 0.1. Then 10 g/L of CS and 4 g/L of WS_2 were rapidly added into the mixed solution. At predetermined time intervals, 0.5 mL of the reaction solution was withdrawn and 0.5 mL of the saturated sodium thiosulfate solution was added to quench the reaction. Finally, the reaction solution was filtered through a polyethersulfone membrane (0.22 μm) for a further analysis.

For the cycle experiments, every 2 hours additional portions of BTA and Cr(VI) were added to the system [34]. Then PDS was added to initiate the next cycle.

2.3. Analytical methods

The residual concentration of BTA was quantified using a HPLC (Alliance) with a UV detector. The mobile phase consisted of 40 % MeOH and 60 % water at the flow rate of 1 mL/min. The detection wavelength was set at 280 nm. Cr(VI) residual concentration was quantified using a UV-vis spectrophotometer (UV-DR6000, HACH, USA) with 1,5-diphenylcarbazide colorimetric method [35]. Methyl phenyl sulfoxide (PMSO) and methyl phenyl sulfone ($PMSO_2$) were analyzed using HPLC. All details about this analytical method are provided in Supporting Information Table S6. After addition of 1,10-phenanthroline, the dissolved Fe^{2+} concentration was determined with UV-vis spectrophotometer at 510 nm. The total iron was determined after addition of hydroxylamine hydrochloride followed by addition of 1,10-phenanthroline. The dissolved Fe^{2+}/Fe^{3+} was measured after filtration, while the total Fe^{2+}/Fe^{3+}, including dissolved and surface-bound species, was measured before filtration [29]. PDS concentration was measured by the KI method [36]. Free radicals were measured using an electron paramagnetic resonance spectroscopy instrument (EPR, Bruker E 500, Germany). TOC analyzer (TOC-V, Shimadzu, Japan) was used to determine the total organic carbon. Method for the detection and identification of BTA degradation products is described in Supporting Information Text S2.

3. Results and discussion

3.1. Characterization of the copper slag

X-ray fluorescence spectroscopy (XRF) was used to determine the chemical components of the CS. As Table S1 shows, the CS used in this study consisted mainly of iron oxides (Fe_2O_3, 50.49 %), SiO_2 (27.62 %), Al_2O_3 (4.09 %), ZnO (3.80 %) and CaO (3.72 %). The mineralogical characterization of the CS was conducted using X-ray infrared diffraction (XRD). The XRD powder diffraction patterns of the initial CS and the used CS are shown in Figure 1A. The main diffraction peaks of the initial CS are typical diffraction peaks of fayalite (Fe_2SiO_4). These results are consistent with previous reports which claimed that the major phase of CS was an iron-calcium-aluminosilicate [37, 38]. The diffraction peaks at 17.27°, 25.17°, 32.10°, 34.30°, 35.26°, 36.06°, 51.67° and 61.00° were assigned to (020), (111), (130), (112), (222) and (242) lattice planes of fayalite, respectively. Scanning electron microscopy (SEM) was applied to characterize the morphology of the CS. As Figure 1B shows, CS particles have irregular structures with different particle sizes. The size of the CS particles is approximately 0.2-20 μm. X-ray photoelectron spectroscopy (XPS) was used to analyze the elemental composition and the variation of valences of the elements on the catalyst's surface. Figure S1A shows that the surface of CS used in this research mainly consists of O, C, Si and Fe. XPS spectra of Fe $2p_{3/2}$ revealed that Fe^{2+} was the major iron species on the surface of the initial CS (Figure S1B), which was consistent with XRD analysis. Nitrogen adsorption and desorption experiments showed that the specific surface area of the CS was only 0.83 m^2/g (Figure S2), and the average pore

size was approximately 2.49 nm. These results indicate that the CS has a very low adsorption capacity for pollutants.

The safety performance of CS was evaluated by toxicity leaching experiment according to the Toxicity Characteristic Leaching Procedure (TCLP) recommended by U.S. Environmental Protection Agency (EPA). The toxicity leaching results are shown in Table S3. The leaching concentrations of all heavy metals in the leaching solution are below the limit of hazardous components specified by the National Standard of China ("Identification standards for hazardous wastes - Identification for extraction toxicity" GB 5085.3—2007). Therefore, according to these results it can be presumed that this CS can be used as an eco-friendly catalyst for Fenton reactions or a heavy metal stabilizer that will not introduce any other pollutants.

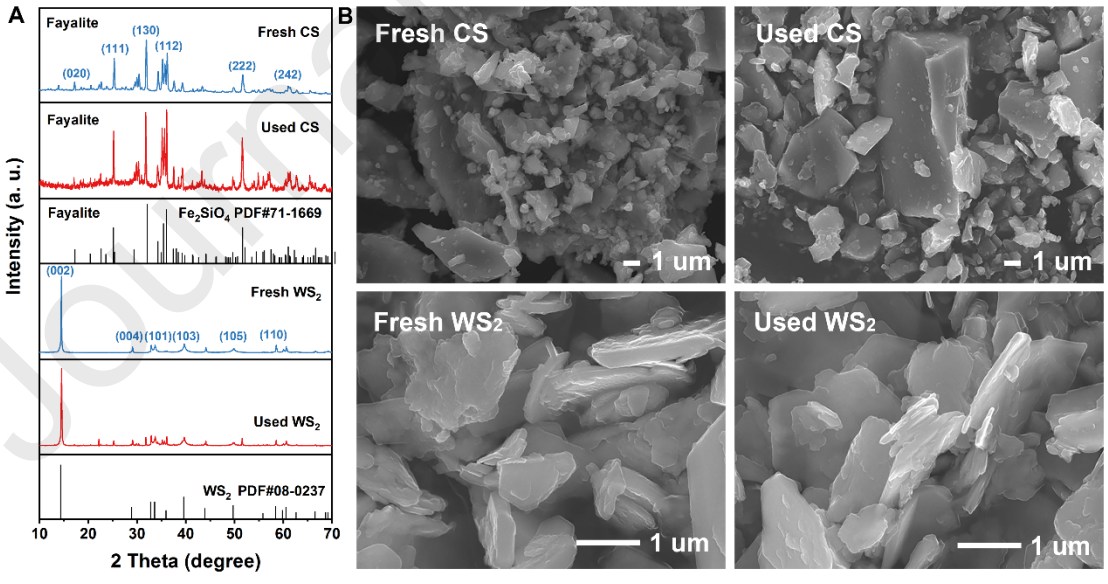

Figure 1. (A) XRD patterns of CS and WS_2 before and after reaction; (B) SEM images of CS and WS_2 before and after reaction.

3.2. WS_2 co-catalytic AOP performance in the degradation of BTA

The performance of the CS/WS_2/PDS system was evaluated with the simultaneous removal of BTA and Cr(VI). Preliminary investigations were conducted in a CS/PDS system, and separately, in the WS_2/PDS system. The purpose of these preliminary experiments was to verify if any of these two systems was able to efficiently remove BTA and Cr(VI). As shown in Figure 2A, the degradation efficiency of BTA in the CS/PDS system was negligible. This observation can be ascribed to two reasons. On the one hand, the spinel structure of fayalite makes dissolution of iron from CS difficult (Figure S3). Moreover, a small amount of ferrous iron leached from CS preferentially donates electrons to Cr(VI). Because, we found that in the absence of Cr(VI), BTA can be removed by about 15% in the CS/PDS system (Figure S4). On the other hand, CS has an extremely low BET surface area of 0.83 m^2/g, which is not conducive to the adsorption and removal of BTA. The removal efficiency of BTA in the WS_2/PDS system was approximately 25 % within 120 min, suggesting that PDS could be slightly activated by WS_2. However, a complete elimination of BTA was achieved within 120 min with 41.9 % TOC removal efficiency in the CS/WS_2/PDS system (Figure S5). The removal rate of BTA in the CS/WS_2/PDS system was approximately 82 times higher than in the CS/PDS system (Figure 2B). Since both, the CS/PDS and WS_2/PDS systems could hardly degrade BTA, WS_2 might enhance the degradation of BTA in the CS/WS_2/PDS system by accelerating the Fenton reaction. The metal sulfide could lower the pH of the system [25], which might induce the iron dissolution and favor the Fenton

reaction. The pH of the CS/WS_2/PDS system decreased continuously from 3.0 to 2.3 throughout the reaction (Figure S6). To investigate the role of decreased pH on the Fenton process, H_2SO_4 was used instead of WS_2 to evaluate the BTA degradation performance in the CS/H_2SO_4/PDS system. The degradation of BTA was slightly increased in the CS/H_2SO_4/PDS system in comparison with the pure CS/PDS system (Figure S7), but still much lower than the degradation rate of BTA in CS/WS_2/PDS system. This result suggested that the decreased pH caused by WS_2 only slightly contributed to the better BTA degradation performance of the CS/WS_2/PDS system.

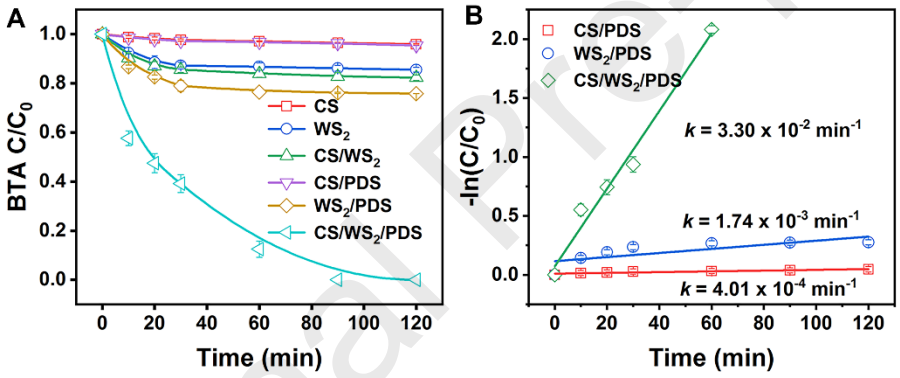

Figure 2. Time profiles of BTA degradation in the mixed system. Reaction conditions: $[BTA]_0$ = 20 mg/L, $[Cr(VI)]_0$ = 20 mg/L, $[PDS]_0$ = 3 mM, $[CS]_0$ = 10 g/L, $[WS_2]_0$ = 4 g/L, pH = 3.0

3.3. Identification of working ROS

3.3.1. Probing free radicals

Sulfate radicals and hydroxyl radicals are generally produced in the process of PDS

196 decomposition mediated by transition metals. *tert*-Butyl alcohol (TBA) can effectively
197 remove •OH. However, TBA is not efficient with $SO_4^{\bullet-}$ due to the different reactivity of
198 TBA with $SO_4^{\bullet-}$ and •OH ($k_{\bullet OH,\ TBA} = (3.8 – 7.6) \times 10^8\ M^{-1}\ s^{-1}$; $k_{SO4\bullet-,\ TBA} = (4 – 9.1) \times$
199 $10^5\ M^{-1}\ s^{-1}$) [39]. Ethanol (EtOH) is usually used to quench both $SO_4^{\bullet-}$ and •OH owing
200 to the high reaction rate of EtOH with both, $SO_4^{\bullet-}$ and •OH ($k_{SO4\bullet-,\ EtOH} = 1.6 – 7.7 \times$
201 $10^7\ M^{-1}\ s^{-1}$; $k_{OH,\ EtOH} = 1.2 – 2.8 \times 10^9\ M^{-1}\ s^{-1}$) [40]. As shown in Figure 3A, the
202 addition of excess of TBA was not able to effectively inhibit the degradation of BTA.
203 The removal efficiency of BTA decreased only from 100 % to 76.5 %, indicating that
204 •OH was not the main ROS in this system. After the addition of 0.1 M EtOH, the
205 removal efficiency of BTA decreased from 100 % to 48.8 %. Notably, EtOH can not
206 only react with hydroxyl radicals and sulfate radicals, but also with other ROS such as
207 Fe(IV) ($k_{Fe(IV),\ EtOH} = 2.51 \times 10^3\ M^{-1}\ s^{-1}$) [41]. Since ethanol inhibited only
208 approximately half of the BTA removal efficiency, it can be presumed that there were
209 some other active species in the system, except for free radicals, which contributed to
210 the degradation of BTA.

211 3.3.2. Probing superoxide radical and singlet oxygen

212 It has been reported that PDS can generate $^1O_2$ in some catalytic reactions, where
213 $O_2^{\bullet-}$ is a precursor of $^1O_2$ [42-45]. Herein, we studied the contribution of superoxide
214 radicals to BTA degradation using *p*-benzoquinone (*p*-BQ) as a quencher of $O_2^{\bullet-}$ ($k_{O_2^{\bullet-},\ p\text{-}BQ} = \sim 10^9\ M^{-1}\ s^{-1}$)
215 [46]. The results in Figure 3B show that 10 mM of *p*-BQ can
216 significantly inhibit the oxidation of BTA. The removal efficiency of BTA decreased

from 100 % to 13.6 %, which indicated that $O_2^{\bullet-}$ was involved in the oxidation of BTA. However, BTA could not be degraded by $O_2^{\bullet-}$ generated from the xanthine/xanthine oxidase system (Figure S8). Furthermore, as shown in Figure S9, no reduction products of NBT were observed at 530 nm, suggesting negligible contribution of $O_2^{\bullet-}$ on the degradation of BTA [47]. Additionally, considering the fact that $O_2^{\bullet-}$ usually originates from dissolved oxygen in the solution, degradation of BTA was also investigated in an inert atmosphere of N_2. A negligible effect of O_2 on the degradation of BTA was observed (Figure S10), suggesting that superoxide radical did not exist in the CS/WS_2/PDS system. Consequently, we assert that $O_2^{\bullet-}$ was not involved in the degradation of BTA in the CS/WS_2/PDS system. A significant inhibition of BTA degradation by *p*-BQ can be explained by a direct consumption of PDS and the competitive depletion of ROS by *p*-BQ (Figures S11 and S12). For example, *p*-BQ also had a significant inhibitory effect on the BTA degradation in the conventional Fenton reaction (Fe^{2+}/H_2O_2 system) (Figure S12), in which hydroxyl radicals are usually considered the primary ROS.

Subsequently, the quenching experiments of $^1O_2$ were performed by adding FFA ($k_{^1O_2, FFA} = 1.2 \times 10^8$ M^{-1} s^{-1}) [31, 48] (Figure 3C). The addition of 10 μM of FFA had a negligible effect on the BTA degradation rate, suggesting that $^1O_2$ was probably not the main ROS in this system. However, after the addition of 0.1 M FFA, the removal rate of BTA was significantly inhibited. The inhibitory rate of BTA degradation caused by FFA addition was higher than 75 %. The phenomenon that FFA had no effect on the

organic pollutant degradation at a low concentration, but a strong inhibitory effect at a high concentration, is similar with conclusions from some previous research [49]. This observation can be explained by the fact that FFA at high concentrations (e.g., 0.1 M) competitively consumed the ROS, resulting in the inhibition of BTA degradation [49]. Indeed, FFA is easily oxidized by various ROS that have high redox potential and even by peroxymonosulfate (PMS) directly, but not by PDS (Figure S13) [50]. The significant inhibitory effect of FFA on BTA degradation in the conventional Fenton reaction (Fe^{2+}/H_2O_2 system) also proved that FFA was easily oxidized by free radicals, in which $^{\bullet}OH$ is considered to be the main ROS (Figure S14). Thus, FFA at high concentrations would lead to the misjudgment of $^1O_2$.

Previous studies that were focused on the singlet oxygen reported that $^1O_2$ had a longer lifetime in D_2O (22 - 70 μs) than in H_2O (2.9-4.6 μs), and that water could act as a scavenger for $^1O_2$ ($k_{H_2O,\,^1O_2} = \sim 10^5\ M^{-1}\ s^{-1}$) [51, 52]. However, water is generally used as the reaction medium. Therefore, the degradation efficiency of a target contaminant would definitely be limited. Luo et al. [53] found that, when the Fenton-like process was performed in D_2O, bisphenol A removal rate increased by 38 %. Thus, in order to further confirm whether $^1O_2$ served as the major ROS in this study, the degradation experiment of BTA was also conducted in D_2O. Unexpectedly, the degradation of BTA hardly changed in D_2O compared to H_2O (Figure 4D). This result further excluded the involvement of $^1O_2$ as a ROS in this system.

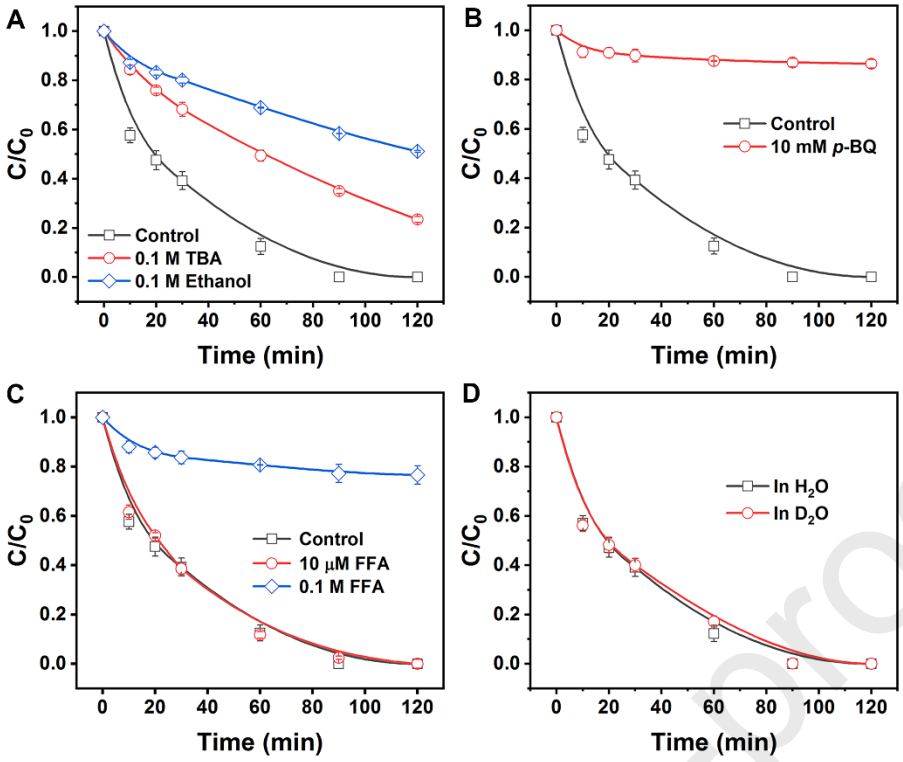

Figure 3. Effects of Ethanol, TBA (A), *p*-BQ (B) and FFA (C) on the degradation of BTA; Time profile of BTA degradation in D_2O (D).

3.3.3. EPR analysis

Electron paramagnetic resonance (EPR) spectroscopy was coupled with 5,5-dimethyl-1-pyrolin-N-oxide (DMPO) as a spin-trapping agent to detect free radicals generated in the CS/WS_2/PDS system (Figure 4A). The signal of DMPO–OH adducts can be clearly observed with typical 1:2:2:1 type characteristic peaks in the CS/PDS system and in the CS/WS_2/PDS system, suggesting the existence of hydroxyl radicals in both of these systems. Nevertheless, the characteristic absorption peaks in the CS/WS_2/PDS system are much higher than in the CS/PDS system. This result indicates that the yield of hydroxyl radicals in the CS/WS_2/PDS system is much higher than in CS/PDS system. Furthermore, the adsorption peaks of hydroxyl radical adducts in the

271 WS_2/PDS system are very weak. Because of that, the significant enhancement of PDS
272 decomposition and hydroxyl radical production should not be ascribed to the activation
273 of PDS by WS_2. Therefore, the accelerated generation of $^{\bullet}OH$ in CS/WS_2/PDS system
274 should be attributed to the accelerated generation of Fe^{2+} after the addition of WS_2. The
275 signal of DMPO–SO_4^{-} adduct was barely found due to its rapid transformation to
276 DMPO–OH adduct. Furthermore, the DMPO–OH adducts could also be produced by
277 the direct oxidation of DMPO by Fe(IV) or singlet oxygen [54, 55].
278 A very weak signal of TEMP–$^1O_2$ adduct in the EPR spectrum also confirmed that
279 a singlet oxygen was not the primary ROS in the CS/WS_2/PDS system (Figure 4B).
280 Although EPR spectra show that $^1O_2$ seems to exist in both CS/PDS and CS/WS_2/PDS
281 systems, BTA can hardly be degraded in the CS/PDS system. The TEMP–$^1O_2$ adduct
282 peaks in the CS/WS_2/PDS system are just slightly higher than those in the CS/PDS
283 system. Obviously, the efficient BTA degradation could not be attributed to $^1O_2$. Nardi
284 et al. [56] found that EPR detection of TEMPO might not be associated with a singlet
285 oxygen production. Excited sensitizer can abstract one electron from TEMP, which
286 leads to the formation of $TEMP^{\bullet+}$, that goes through deprotonation and combination
287 with dissolved oxygen to form TEMPO. These processes might be responsible for
288 appearance of weak TEMP–$^1O_2$ adduct peaks in the CS/PDS and CS/WS_2/PDS systems.
289 Therefore, $^1O_2$ was excluded as the major ROS responsible for BTA degradation.
290

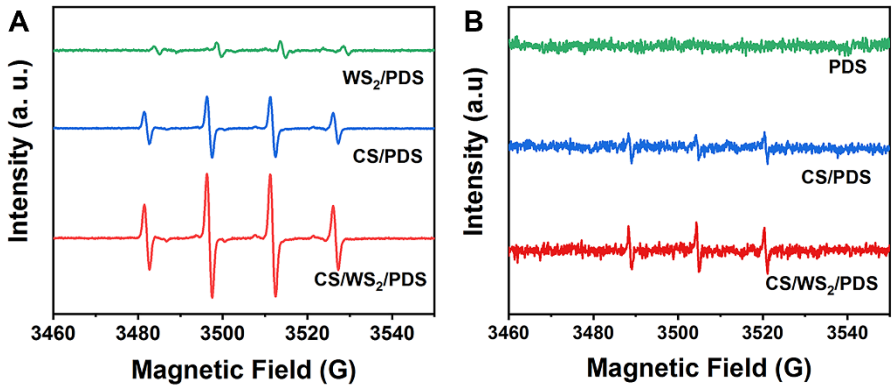

Figure 4. (A) TMPO trapped EPR spectra of hydroxyl radical/sulfate radical and (B) TEMP trapped EPR spectra of singlet oxygen at different conditions.

3.3.4. Probing Fe(IV)-oxo (ferryl) species

Some studies have found that Fe(IV)-oxo (ferryl) species are the main non-radical ROS in iron-based materials mediated AOPs [57-59]. PMSO was usually chosen as a probe compound to verify the existence of Fe(IV), because it could be oxidized by Fe(IV) to generate $PMSO_2$ through the oxygen atom transfer mode [60]. This is a reaction that clearly distinguishes free radicals and Fe(IV). Because of that, the oxidation behavior of PMSO and the yield of $PMSO_2$ in the CS/WS_2/PDS system were investigated. As shown in Figure 5A, PMSO was gradually degraded in 60 min, with the removal efficiency of 91.4 %. Interestingly, we found that the degradation of PMSO was accompanied by the obvious generation of $PMSO_2$. The yield of $PMSO_2$ (η ($PMSO_2$), the molar ratio of $PMSO_2$ produced to PMSO decreased) was quantified to be 0.67 over the reaction time (Eq 1) (Figure S15). These results suggested that Fe(IV) could be generated in the CS/WS_2/PDS system at acidic pH (Eq 2), which might be the

main cause for the degradation of BTA. Raman spectrum was recorded to confirm the generation of Fe(IV) in the CS/WS_2/PDS system (Figure 5B). A new peak emerged at ~ 698 cm^{-1} in the CS/WS_2/PDS system, which could be attributed to Fe(IV) generated from the oxidation of Fe^{2+} [29]. Furthermore, DMSO generally functions as both, an •OH scavenger and an O-atom acceptor [61, 62]. Moreover, PDS do not react with PMSO (Figure S16). As Figures 5C and D show, the addition of DMSO showed an evident inhibition on the degradation efficiency and kinetics of BTA. The removal efficiency of BTA decreased from 100 % to 10.7 %. Since •OH has been confirmed to have a relatively low contribution to the degradation of BTA, it can be concluded that Fe(IV) primarily contributed to the degradation of BTA.

$$\eta = \frac{\Delta PMSO_2}{\Delta PMSO} \quad (1)$$

$$Fe^{2+} + S_2O_8^{2-} \rightarrow Fe^{IV}O^{2+} + 2SO_4^{2-} \quad (2)$$

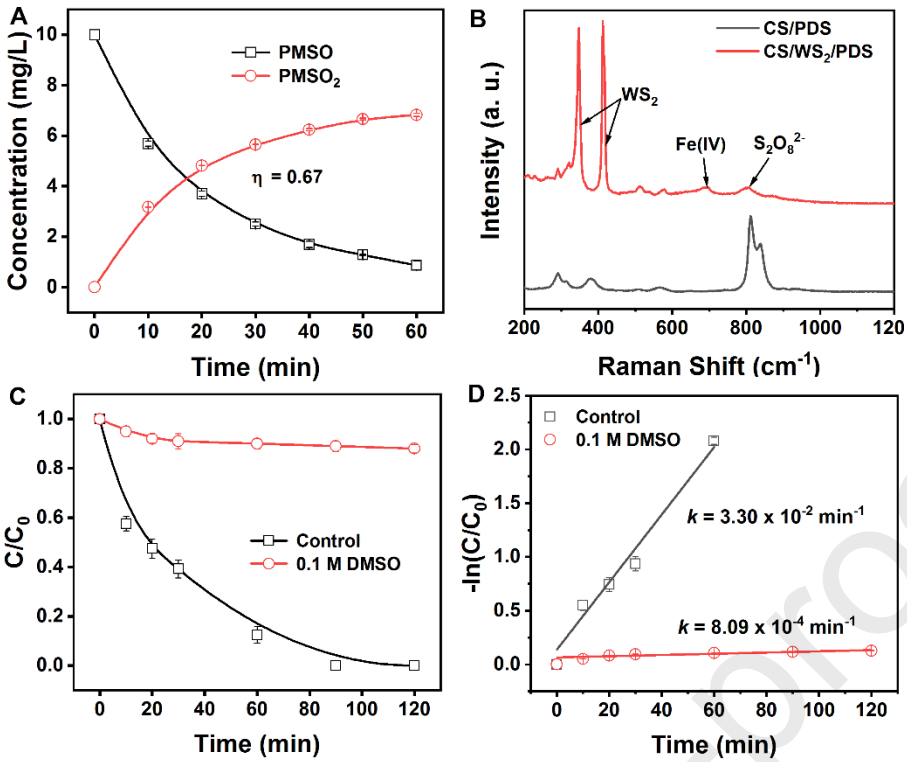

321

322 **Figure 5**. (A) The degradation of PMSO and generation of $PMSO_2$ in the $CS/WS_2/PDS$

323 system (Reaction conditions: $pH_{initial}$ = 3.0, $[PMSO]_0$ = 10 mg/L, $[PDS]_0$ = 3 mM, $[CS]_0$

324 = 10 g/L, $[WS_2]_0$ = 2 g/L); (B) Raman spectra of CS and CS/WS_2 mixture; (C) Time

325 profiles of BTA degradation with or without DMSO; (D) Plots of $-\ln(C/C_0)$ versus time

326 for the degradation of BTA with or without DMSO.

327 3.4. Kinetics calculation

328 To further determinate the relative contributions of $SO_4^{\bullet-}$, $^{\bullet}OH$ and Fe(IV) during

329 BTA degradation, based on the previous studies [29, 30], the kinetics experiments were

330 conducted in the mixed system which included nitrobenzene (NB), benzoic acid (BA)

331 and BTA. According to the reported second-order rate constants for reactions of free

332 radicals with these three probe compounds (Table S4) and kinetic experimental results

333 (Figure S17), the steady-state concentrations of $^{\bullet}OH$ and $SO_4^{\bullet-}$ were calculated. The

steady state concentration of Fe(IV) was determined according to the kinetics of $PMSO_2$ generation from the oxidation of PMSO (Figure S18). The detailed calculation processes were shown in Supporting Information Text S3. The steady-state concentrations of •OH and $SO_4^{\bullet-}$ in the CS/WS_2/PDS system were calculated to be 4.36 × 10^{-14} M and 1.1 × 10^{-13} M, respectively. The steady-state concentration of Fe(IV) was calculated to be 3.60 × 10^{-9} M. Obviously, the steady-state concentration of Fe(IV) is much higher than the concentrations of •OH or $SO_4^{\bullet-}$. This result is consistent with the quenching experiments of ROS. Taking into account the reaction selectivity of ROS to different organic compounds, the relative contributions of free radicals and non-radical ROS were evaluated. This evaluation was based on the calculated steady-state concentrations of ROS and reported second-order rate constants of free radicals towards BTA. The relative contributions of •OH, $SO_4^{\bullet-}$ and Fe(IV) in the CS/WS_2/PDS were estimated to be 27.7 %, 8.9 % and 63.4 %, respectively, based on the Eqs 3 - 16. These results further indicated that Fe(IV) was the primary ROS responsible for the degradation of BTA.

$$k_{obs,\,NB}t = k_{\bullet OH,\,NB}[\bullet OH]_{ss}\,t \quad (3)$$

$$k_{obs,\,BA}t = k_{\bullet OH,\,BA}[\bullet OH]_{ss}t + k_{SO4\bullet-,\,BA}\left[SO_4^{\bullet-}\right]_{ss}t \quad (4)$$

$$k_{obs,\,BTA}t = k_{\bullet OH,\,BTA}[\bullet OH]_{ss}t + k_{SO4\bullet-,\,BTA}\left[SO_4^{\bullet-}\right]_{ss}t + k_{Fe(IV),\,BTA}[Fe(IV)]_{ss}\,t \quad (5)$$

$$[\bullet OH]_{ss} = \frac{k_{obs,\,NB}}{k_{\bullet OH,\,NB}} \quad (6)$$

$$[SO_4^{\bullet-}]_{ss} = \frac{k_{obs,BA} - k_{\bullet OH,BA}[\bullet OH]_{ss}}{k_{SO4\bullet-,BA}} \quad (7)$$

$$\frac{d[PMSO_2]}{dt} = -k_{PMSO,Fe(IV)}[Fe(IV)]_{ss}[PMSO] \quad (8)$$

$$= \frac{\Delta\, PMSO_2}{\Delta\, PMSO} = \frac{[PMSO_2]}{[PMSO]_0 - [PMSO]} \quad (9)$$

Substitution of Eq 13 into Eq 14 yields:

$$\frac{d[PMSO_2]}{[PMSO]_0 - \frac{1}{\eta}[PMSO_2]} = k_{PMSO,\ Fe(IV)}[Fe(IV)]_{ss}dt \quad (10)$$

Integrating Eq 15 can yield:

$$ln\frac{[PMSO]_0}{[PMSO]_0 - \frac{1}{\eta}[PMSO_2]} = ln\frac{[PMSO]_0}{[PMSO]} = k_{PMSO,\ Fe(IV)}[Fe(IV)]_{ss}t = -k_{obs}t \quad (11)$$

$$[Fe(IV)]_{ss} = \frac{k_{obs}}{k_{PMSO,Fe(IV)}} \quad (12)$$

$$[\mathrm{Fe(IV)}]_{ss} = \frac{k_{obs,PMSO}}{k_{Fe(IV),PMSO}} \quad (13)$$

$$R_{\bullet OH} = \frac{k_{\bullet OH,BTA}[\bullet OH]_{ss}}{k_{obs,BTA}} \quad (14)$$

$$R_{SO_4^{\bullet-}} = \frac{k_{SO_4^{\bullet-},BTA}[SO_4^{\bullet-}]_{ss}}{k_{obs,BTA}} \quad (15)$$

$$R_{Fe(IV)} = 1 - R_{\bullet OH} - R_{SO_4^{\bullet-}} \quad (16)$$

Where $[^{\bullet}OH]_{ss}$, $[SO_4^{\bullet-}]_{ss}$ and $[Fe(IV)]_{ss}$ are the steady-state concentrations of $^{\bullet}OH$, $SO_4^{\bullet-}$ and Fe(IV), respectively; k_{obs} is the pseudo-first-order rate constant; η is the yield of $PMSO_2$; $R_{\bullet OH}$, $R_{SO_4^{\bullet-}}$ and $R_{Fe(IV)}$ are the relative contributions of $^{\bullet}OH$, $SO_4^{\bullet-}$ and Fe(IV) on the oxidation of BTA, respectively.

3.5. Mechanisms of BTA degradation promoted by WS_2

To further confirm the acceleration of the Fenton reaction by WS_2, the decomposition of PDS was monitored. In the CS/PDS system, less than 5 % of the PDS was consumed within 120 min, whereas the introduction of WS_2 greatly increased the decomposition efficiency of PDS to 66 % within 120 min (Figure S19a). The

decomposition of PDS fitted well with pseudo-first order kinetic model (Figure S19b), and the apparent rate constant (k) of PDS decomposition increased by 161 times from 5.18×10^{-5} min^{-1} in the CS/PDS system to 8.33×10^{-3} min^{-1} in the CS/WS_2/PDS system. In addition, the significantly enhanced characteristic adsorption peaks of EPR spectra trapped by DMPO also indicated that the introduction of WS_2 accelerated the Fenton reaction and ROS production (Figure 4a).

Although all previous results showed that WS_2 could indeed accelerate the Fenton reaction process in the CS/WS_2/PDS system, it remained unclear how actually WS_2 affected this process. It could be presumed that the introduction of WS_2 accelerated the Fenton reaction in two ways: (1) WS_2 catalyzed the decomposition of PDS; (2) WS_2 acted as a reducing agent to accelerate the Fe^{3+}/Fe^{2+} cycle in the system, thus promoting the decomposition of PDS. To test this hypothesis, 1,10-phenanthroline and F^- were used as masking agents for Fe^{2+} and Fe^{3+} in the system, respectively. The aim was to investigate whether the iron ions released from the copper slag and iron cycling play a key role in the degradation of BTA. As Figure 6A shows, upon the addition of 1,10-phenanthroline, BTA degradation was almost completely inhibited. These results indicated that the direct depletion of PDS by 1,10-phenanthroline can be excluded (Figure S20). Therefore, these results suggested that Fe^{2+} did play a key role in the BTA degradation in the CS/WS_2/PDS system. The results also negated the hypothesis that the accelerated Fenton reaction after the introduction of WS_2 might be due to the direct activation of PDS by WS_2.

In the section 3.2 was demonstrated that the pH decrease after the introduction of WS_2 in the system only slightly contributed to the accelerated Fenton reaction. These results also indicated that the Fe^{2+} ions in the system probably originated from the conversion of Fe^{3+} by WS_2 rather than from dissolution from CS. To further confirm if Fe^{3+}/Fe^{2+} transformation had a crucial role in the degradation of BTA, F^- (KF) was used as a masking agent for Fe^{3+} to disrupt the Fe^{3+}/Fe^{2+} cycle. As shown in Figure 6B, the addition of F^- significantly inhibited the degradation of BTA in the $CS/WS_2/PDS$ system, and indicated that the accelerated Fe^{3+}/Fe^{2+} cycle was indeed crucial in the degradation of BTA. The color change of the supernatant after the reaction also revealed the difference of iron species in different systems (Figure S21). It can be observed that the color of the supernatant is orange-red due to the high concentration of Fe^{3+} in the CS/PDS system, whereas the supernatant after the reaction in the $CS/WS_2/PDS$ system is basically colorless.

Dissolved iron species variation was monitored to further investigate the Fe^{3+}/Fe^{2+} transformation in the $CS/WS_2/PDS$ system (Figure 6C). In the CS/PDS system, Fe^{2+} was almost undetectable during the whole reaction process, while Fe^{3+} concentration increased gradually in the first 20 min and then remained constant. This result can be attributed to the formation of an iron oxide passivation layer on the surface of the catalyst, which deactivated the catalyst and prevented contact between Fe^{3+} and the catalyst. In the case of the $CS/WS_2/PDS$ system, Fe^{2+} concentration increased continuously over time. The maximum concentration of dissolved Fe^{2+} reached 18.67

mg/L, which was much higher than in the CS/PDS system. Obviously, the introduction of WS_2 facilitated not only the transformation from Fe^{3+} to Fe^{2+}, but also the release of iron species from CS by preventing the formation of the iron oxide passivation layer. Furthermore, the Fe^{2+}/Fe^{3+} ratio continued to increase over time (Figure 6D). Additionally, a good positive relationship between Fe^{2+}/Fe^{3+} ratio and BTA removal efficiency also revealed a high efficiency of WS_2 in acceleration of the Fe^{3+}/Fe^{2+} cycling and BTA degradation (Figure S22). XPS spectra of W 4f was recorded in order to certify the reduction of Fe^{3+} by W^{4+}. As it is shown in Figure 6E, two distinct characteristic peaks of used WS_2 at 35.1 eV and 37.5 eV were observed. These peaks could be ascribed to the W(VI) $4f_{5/2}$ and W(VI) $4f_{7/2}$, while the peaks at approximately 32.5 eV and 34.6 eV were assigned to W(IV) $4f_{5/2}$ and W(IV) $4f_{7/2}$, respectively [25]. Obviously, the W^{6+} content on the surface of WS_2 increased after reaction in comparison with fresh WS_2 (from 15.8 % to 30.7 %), which further indicated that W^{4+} on the surface of WS_2 was oxidized to W^{6+} by Fe^{3+} (Eq 17).

$$Fe^{3+} + W^{4+} \rightarrow Fe^{2+} + W^{6+} \quad (17)$$

S^{2-} in the system might also have contributed to the Fe^{3+}/Fe^{2+} conversion. Previous study on the promotion of the iron cycle by WS_2 found that the reduction ability of WS_2 to Fe^{3+} was much stronger than that of WO_2. Reducing S species served as an electron donor and enhanced the regeneration of Fe^{2+} [63]. Furthermore, the reducing S species in pyrite also generally acts as an electron donor for Fe^{3+} to promote iron cycling [64, 65]. Thus to confirm the contribution of reducing S species in the generation of Fe^{2+}, S

438 2p XPS spectra were analyzed. As shown in Figure S23, S^{2-} was the major species in
439 the fresh WS_2, whereas a new peak emerged at ~ 163.6 eV in the used WS_2, which was
440 assigned to S^0. Obviously, S^{2-} served as electron donor that also participated in the
441 regeneration of Fe^{2+} (Eq 18).

442 $$Fe^{3+} + S^{2-} \rightarrow Fe^{2+} + S^0 \quad (18)$$

443 Subsequently, the interfacial behavior of the Fe^{3+}/Fe^{2+} transformation was
444 investigated by monitoring dissolved iron species and surface-bound iron species. As
445 shown in Figure 6F, it was found that surface Fe^{2+} was much higher in concentration
446 than dissolved Fe^{2+} in the CS/WS_2/PDS system, which means that the Fe^{3+}/Fe^{2+}
447 conversion should occur on the surface of WS_2 or CS. Owing to the fact that WS_2 is
448 insoluble in aqueous solution, but WS_2 is the only electron donor of Fe^{3+}, it can be
449 concluded that the Fe^{3+}/Fe^{2+} cycle primarily occurred on the surface of WS_2. Since the
450 zero charge point of WS_2 is located at pH = 2.2 [25], WS_2 is negatively charged in the
451 CS/WS_2/PDS system due to the deprotonation, which is favorable for the adsorption of
452 Fe^{3+} (The pH of the solution decreases from 3.0 to 2.4 throughout the reaction). In spite
453 of the fact that Fe^{3+}/Fe^{2+} occurred around the surface of WS_2, the activation of PDS and
454 degradation of BTA should be assigned to a homogeneous processes. Since WS_2 is
455 usually negatively charged, absorption of PDS ($S_2O_8^{2-}$) on the surface of WS_2 is
456 prevented by the electrostatic repulsion. Fe^{2+} produced on the surface of WS_2 is
457 dissolved further into the solution due to high solubility, and these dissolved Fe^{2+} ions
458 dominate the PDS decomposition. The degradation of BTA in the Fe^{2+}/WS_2/PDS and

459 Fe^{3+}/WS_2/PDS systems was conducted to analyze this process. The concentrations of
460 Fe^{2+} and Fe^{3+} were set as 1.65 mg/L and 4.0 mg/L respectively, which are consistent
461 with the dissolved Fe^{2+} and Fe^{3+} concentrations in the CS/WS_2/PDS system at 60 min.
462 The results showed that both Fe^{2+}/WS_2/PDS and Fe^{3+}/WS_2/PDS systems achieved
463 efficient BTA degradation within 120 min (Figure S24). These results suggest that an
464 efficient PDS activation and BTA degradation can be achieved through the acceleration
465 of the homogeneous Fe^{3+}/Fe^{2+} cycle by WS_2, even at low iron ion concentrations. It is
466 noteworthy that the degradation rate of BTA in both Fe^{2+}/WS_2/PDS and Fe^{3+}/WS_2/PDS
467 systems was higher than that in CS/WS_2/PDS system, which may be due to a very low
468 level of dissolved iron in the CS/WS_2/PDS system at the beginning of the reaction.

469 Scheme 1 illustrates the co-catalytic mechanisms of WS_2 in the CS/PDS Fenton
470 reactions. Firstly, Fe^{3+} in aqueous solution absorbs on the surface of WS_2 due to the
471 electrostatic attraction. Subsequently, Fe^{3+} adsorbed on the surface of WS_2 is reduced
472 to Fe^{2+} by W^{4+} (Eq 20), while the surface W^{4+} is oxidized to W^{6+}. Then, the produced
473 Fe^{2+} on the surface of WS_2 dissolves further into the solution due to its high solubility.
474 And then, PDS is activated by dissolved Fe^{2+} to produce Fe(IV) and free radicals to
475 attack BTA. Finally, Fe^{3+} produced in the system participates in the next cycle.

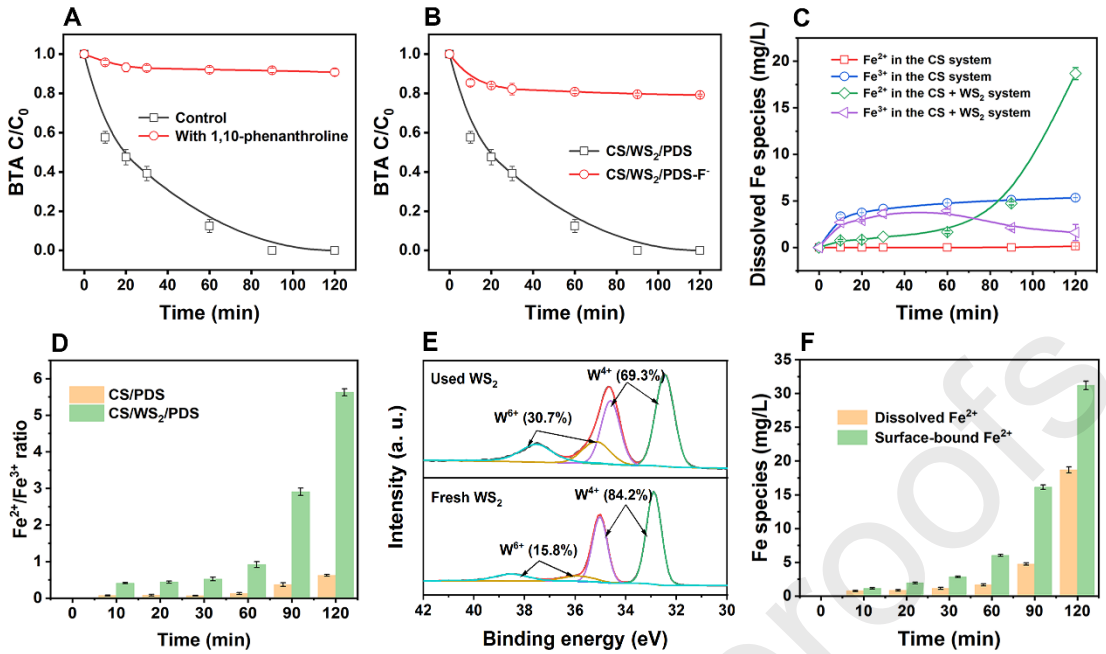

476

477 **Figure 6**. (A) Effect of 1,10-phenanthroline on the degradation of BTA; (B) Effect of

478 KF on the degradation of BTA; (C) Time profiles of iron species concentrations

479 (dissolved Fe and surface-bound Fe); (D) The dissolved Fe^{2+}/Fe^{3+} ratio in the different

480 systems; (E) The W 4f XPS spectra of WS_2 before and after use; (F) Comparison of

481 dissolved Fe^{2+} and surface-bound Fe^{2+} concentrations in the $CS/WS_2/PDS$ system.

482 Reaction conditions: $[BTA]_0$ = 20 mg/L, $[PDS]_0$ = 3 mM, $[CS]_0$ = 10 g/L, $[WS_2]_0$ = 4

483 g/L, $[1,10\text{-phenanthroline}]_0$ = 0.1 M, $[KF]_0$ = 0.1 M, $pH_{initial}$ = 3.0.

484

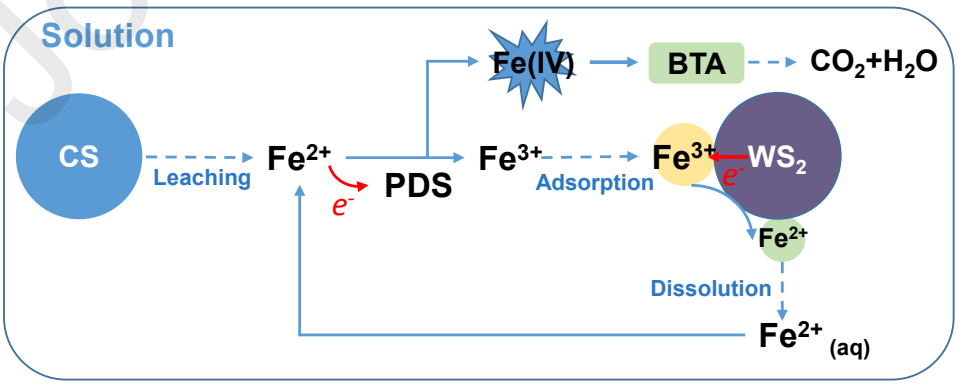

485

Scheme 1. WS_2 accelerated Fe^{3+}/Fe^{2+} cycle to promote the Fenton reaction's efficiency.

3.6. BTA degradation products

Possible degradation products of BTA in CS/WS_2/PDS system were detected using a GC-MS. The products of BTA degradation can be divided into two categories: compounds produced by electron transfer and compounds produced by oxygen atom transfer. The main compounds formed are: 1-hydroxybenzotriazole, phenylhydrazine, aniline, nitrosobenzene, nitrobenzene, azobenzene and azoxybenzene. The possible degradation pathways of BTA in the CS/WS_2/PDS Fenton system are proposed in Figure 7. The first step was mainly hydroxylation of the pyridine ring in BTA to generate 1-hydroxybenzotriazole. This product could be further oxidized by the rupture of the pyridine ring, resulting in the generation of phenylhydrazine and aniline. On the one hand, aniline could be oxidized to nitrosobenzene by oxygen atom transfer. On the other hand, two molecules of aniline could be linked to form azobenzene, which could be further oxidized to azoxybenzene through the oxygen atom transfer. The specific MS spectra of the BTA degradation products in the CS/WS_2/PDS system are shown in Figure S25. Interestingly, there are some degradation intermediates generated via transfer of oxygen atom, which seem to be different from those that were expected to be formed from $SO_4^{\bullet-}$ and/or $^{\bullet}OH$ mediated oxidation. This result further suggests that Fe(IV) should be the primary ROS that was responsible for the degradation of BTA.

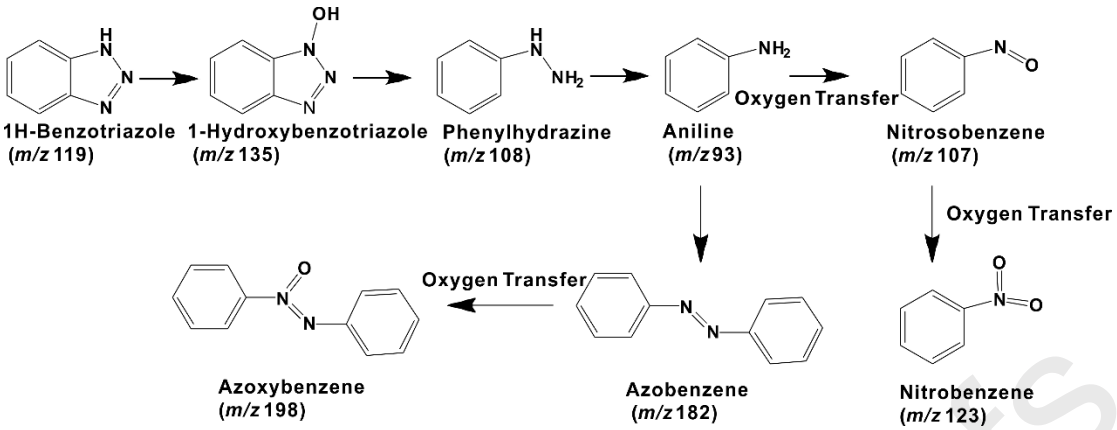

505

506 **Figure 7.** The proposed degradation pathway of BTA in the CS/WS_2/PDS system.

507

508 3.7. WS_2 accelerated reduction of Cr(VI)

509 Cr(VI) is a toxic metal that is widespread in aqueous environments. Treatment of
510 Cr(VI) in waste water and drinking water has been a great challenge. Coexistence of
511 Cr(VI) and organic pollutants in the environment is a common phenomenon. Because
512 of that, there is a great need for the development of a system that will be able to
513 simultaneously eliminate Cr(VI) and organic pollutants. In this study, WS_2 was used as
514 a co-catalyst for simultaneous removal of Cr(VI) and BTA in the CS/WS_2/PDS system.
515 As it was explained earlier, preliminary investigations were conducted in the CS/PDS
516 system, and, separately, in the WS_2/PDS system. As Figure 8 shows, CS/WS_2/PDS
517 system showed a remarkable promotion of Cr(VI) reduction, in comparison with the
518 CS/PDS system. Despite the major iron species of CS is ferrous iron (Fe_2SiO_4, fayalite),
519 CS/PDS system had a very low reduction rate of Cr(VI). This result can be explained
520 with a very stable spinel structure of fayalite in which iron ions are surrounded by a
521 silicon-oxygen tetrahedral or octahedral lattice. Because of that, iron ions in CS are

522 difficult to be released and used. Moreover, the slow Fe^{3+}/Fe^{2+} cycle also inhibited the
523 reduction of Cr(VI). A moderate reduction efficiency of Cr(VI) was obtained in the
524 WS_2/PDS system. Cr(VI) could not be completely reduced by WS_2 even in a high
525 dosage (4 g/L). As it is well known, Cr(VI) usually exists in the form of oxyanions in
526 aqueous solution ($Cr_2O_7^{2-}$ or CrO_4^{2-}) (Figure S26). The surface of WS_2 in the
527 CS/WS_2/PDS system is negative charged due to the deprotonation which causes
528 electrostatic repulsion between WS_2 and Cr(VI) and hinders reduction of Cr(VI)
529 Because of that, in this system Cr(VI) preferably reacts with Fe^{2+} due to the electrostatic
530 attraction. Furthermore, WS_2 preferably reacts with Fe^{3+} to generate Fe^{2+} which is
531 confirmed by a constantly elevated Fe^{2+} concentration in the system (Figure 6C and D).
532 In order to further understand the mechanisms of Cr(VI) reduction, Cr(VI)
533 reduction experiments were conducted without BTA (Figure 8B). The results showed
534 that Cr(VI) cannot be reduced by PDS, which reacts differently than H_2O_2. As it is well
535 known, Cr(VI) can be quickly reduced by H_2O_2 in acidic conditions. Moreover,
536 previous studies reported that H_2O_2 could be activated by both Cr(VI) and
537 $[Cr^{III}(H_2O)_y](OH)_x$ to generate $^{\bullet}OH$, which was used in degradation of 4-chlorophenol
538 [8, 66]. However, Cr(VI) can hardly activate PDS due to the more stable SO_3-O-O-SO_3
539 structure. Even PDS is unable to reduce Cr(VI) due to the high redox potential [E^0
540 ($S_2O_8^{2-}/SO_4^{2-}$) = 2.01 eV] (Figure 8B). Approximately 20 % of Cr(VI) was reduced by
541 CS alone. However, the addition of CS and WS_2 to the reaction system made the
542 reduction efficiency of Cr(VI) higher than 70 % in 10 min. As discussed above, the

addition of WS_2 not only accelerated the Fe^{3+}/Fe^{2+} cycle, but also the dissolution of Fe^{2+} due to the decreased solution pH. Fe^{2+} preferably reacts with Cr(VI) than with WS_2 due to the electrostatic attraction. Furthermore, a significant positive correlation between production of Fe^{2+} and reduction of Cr(VI) further confirms that Fe^{2+} in the system has a key role for the reduction of Cr(VI) (Figure 8C). In order to confirm whether the Fe^{3+}/Fe^{2+} cycle accelerated by WS_2 had a main role in the Cr(VI) reduction process, F^- (KF) was used as a masking agent for Fe^{3+}, to disrupt the Fe cycle in this system. F^- is able to form FeF_3 precipitate with Fe^{3+}, while F^- cannot be oxidized by PDS due its chemical stability. The effect of F^- on the reduction of Cr(VI) in the CS/WS_2/PDS system is shown in Figure 8D. The addition of F^- significantly inhibited the reduction efficiency of Cr(VI) in the CS/WS_2/PDS system (reduced by 50.2%), which should be ascribed to the destruction of Fe^{3+}/Fe^{2+} cycle through the formation of FeF_3 precipitate. Moreover, the reduction efficiency of Cr(VI) in the CS/WS_2/PDS-F^- system was even lower than that in the WS_2/PDS system. The reduction of Cr(VI) in the CS/WS_2/PDS-F^- system almost stopped after 10 min. This result can be explained with the formation of a dense FeF_3 passivation layer on the surfaces of WS_2 and CS, which interrupts the electron transfer between WS_2/Fe^{2+} and Cr(VI). As it is shown earlier, the Fe^{3+}/Fe^{2+} cycle does play a crucial role in the reduction of Cr(VI), in which WS_2 acts as an electron donor to facilitate the efficient conversion of Fe^{3+} to Fe^{2+}.

Finally, the XPS spectrum was employed to the detect the reduction products of Cr(VI). As it is shown in Figure S27, Cr(III) was identified as the main reduction

product of Cr(VI) in the reaction system used. Since the solution pH < 3.0, soluble Cr^{3+} was the main species of Cr(III), rather than $FeCr_2O_4$ or Cr_2O_3 precipitates (Figure S28).

We have demonstrated that iron ions played the main roles during the reduction of Cr(VI) in the CS/WS_2/PDS system. To further investigate whether the Cr(VI) reduction was dominated by homogeneous or heterogeneous reactions, the Zeta potential of the copper slag was measured. As it is shown in Figure S29, the zero charge point of copper slag is at pH = 2.2. Because of that, the copper slag surface is negatively charged throughout the reaction due to the deprotonation in the CS/WS_2/PDS system. Obviously, this is unfavorable for the contact reduction of Cr(VI) due to electrostatic repulsion. Furthermore, WS_2 surface is also negatively charged due to its low zero potential point (pH_{pzc} = 2.2) and deprotonation. This also negates the contact reduction of Cr(VI) on the surface of WS_2. According to all these facts it can be presumed that the reduction of Cr(VI) in the CS/WS_2/PDS system is dominated by the homogeneous Fe^{2+}. To confirm this presumption, Cr(VI) reduction in the Fe^{2+}/WS_2/PDS and Fe^{3+}/WS_2/PDS systems was performed (Figure S30). The concentrations of Fe^{2+} and Fe^{3+} were set as 1.65 mg/L and 4.0 mg/L respectively, which are consistent with the dissolved Fe^{2+} and Fe^{3+} concentrations in the CS/WS_2/PDS system at 60 min. The results showed that both Fe^{2+}/WS_2/PDS and Fe^{3+}/WS_2/PDS systems achieved efficient Cr(VI) reduction within 120 min, which is generally in agreement with the results in the CS/WS_2/PDS system. In other words, the homogeneous iron is able to achieve efficient Fe^{3+}/Fe^{2+} conversion and Cr(VI) reduction with the assistance of WS_2, even at a very low dissolved iron

585 content.

586 According to the previous discussion, it can be claimed that the reduction of Cr(VI)
587 in the CS/WS_2/PDS system mainly occurred in the solution through homogeneous
588 reactions, while the Fe^{3+}/Fe^{2+} transformation primarily occurred on the surface of WS_2,
589 as it is shown in Scheme 2. Firstly, Fe^{3+} generated from the oxidation of Fe^{2+} by Cr(VI)
590 absorbs on the surface of WS_2. Then WS_2 surface produces H_2S to expose W^{4+}. W^{4+}
591 preferentially provides electrons to Fe^{3+}, rather than to Cr(VI), due to the electrostatic
592 repulsion between WS_2 and Cr(VI). Subsequently, the Fe^{2+} produced on the surface of
593 WS_2 dissolves back into solution to reduce Cr(VI). Additionally, surface W^{4+} can also
594 directly donate electrons to Cr(VI) around the WS_2 surface.

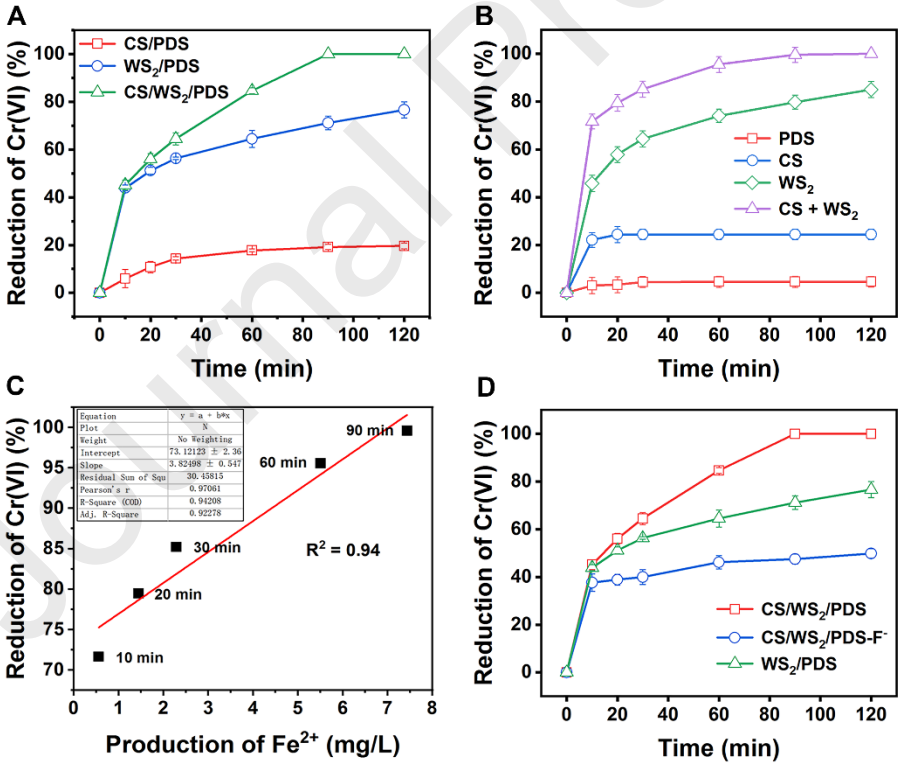

595

596 **Figure 8.** (A) Reduction of Cr(VI) in the mixed systems; (B) Reduction of Cr(VI)
597 without BTA; (C) Reduction of Cr(VI) and production of Fe^{2+} without BTA; (D) Effect

598 of F^- on the reduction of Cr(VI), $[Cr(VI)]_0$ = 20 mg/L, $[BTA]_0$ = 20 mg/L, $[CS]_0$ = 10

599 g/L, $[WS_2]_0$ = 4 g/L, $[KF]_0$ = 0.1 M, $pH_{initial}$ = 3.0.

600

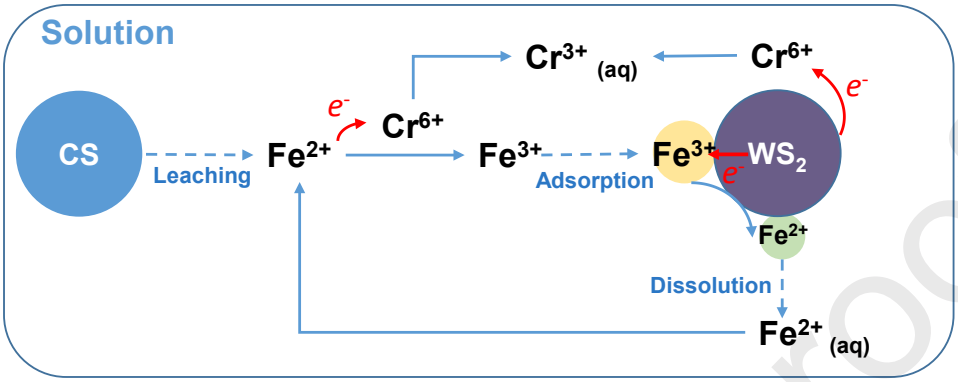

601

602 **Scheme 2.** WS_2 promoted reduction of Cr(VI).

603

604 3.8. Influencing factors affecting the removal of BTA and Cr(VI)

605 The impacts of pH, PDS concentration and water matrix on the BTA degradation

606 and Cr(VI) reduction were evaluated. As it is shown in Figure 9A and B, both, the BTA

607 degradation and Cr(VI) reduction were sensitive to the solution pH. BTA degradation

608 gradually decreased as the initial solution pH raised from 3 to 10. Obviously, acidic

609 solution pH was more favorable to BTA degradation than neutral or alkaline conditions.

610 Lower pH accelerates the release of iron ions from CS, which is favorable for both, the

611 PDS decomposition and BTA removal. On the contrary, one part of iron ions will

612 precipitate at neutral or alkaline pH, which has an adverse effect on the PDS

613 decomposition. In case of Cr(VI) reduction, acidic solution pH is also more favorable

614 than neutral or alkaline conditions. On the one hand, acidic conditions would bring out

more dissolved iron ions from the CS. On the other hand, when the solution pH is lower than the zero charge point of the CS, the surface of the CS will have a positive charge due to the protonation. This situation is more conducive to the removal of Cr(VI) by electrostatic attraction between the CS and Cr(VI) oxygen-containing anions ($Cr_2O_7^{2-}$ or CrO_4^{2-}). PDS concentration can also influence the degradation efficiency of BTA. BTA degradation efficiency increased with the PDS concentration in the CS/WS_2/PDS system (Figure 9C). Furthermore, the kinetic parameters were well fitted with the pseudo-first-order model, while the apparent rate constant (k_{obs}) was linearly correlated with PDS concentration (Figure S31A and B). Hence, the BTA degradation is of the first-order with regard to PDS concentration. Interestingly, increased initial PDS concentration also resulted in an improved Cr(VI) removal (Figure 9D). This result could be ascribed to the increased H^+ concentration that derived from PDS decomposition, which could facilitate the dissolution of iron ions from the CS. Meanwhile, the enhanced surface protonation of the CS also increased electrostatic attraction between Cr(VI) and the CS. As a consequence, the removal efficiency of Cr(VI) was increased.

The simultaneous removal of BTA and Cr(VI) in a real water (mine water, river water and tap water) was also investigated (Figures 9E and F). The degradation rate of BTA was obviously inhibited in the real water. The decreased Fenton reaction rate in a real water of CS/WS_2/PDS system could be attributed to the competitive consumption of ROS by complex ingredients in real water (Table S5), such as dissolved organic

matter and interfering ions. Tap water had the most significant effect on the BTA degradation. This observation might be ascribed to the consumption of ROS by the high concentration of chloride ions (Table S5). In case of Cr(VI) removal, a similar trend was found in the real water. This result could be attributed to consumption of Fe^{2+} and W^{4+} by oxidizing species in a real water (e.g., nitrite or nitrate). Fortunately, good removal efficiency can still be achieved in 120 min except for the tap water. These results suggested that the CS/WS_2/PDS is a promising system for wastewater treatment.

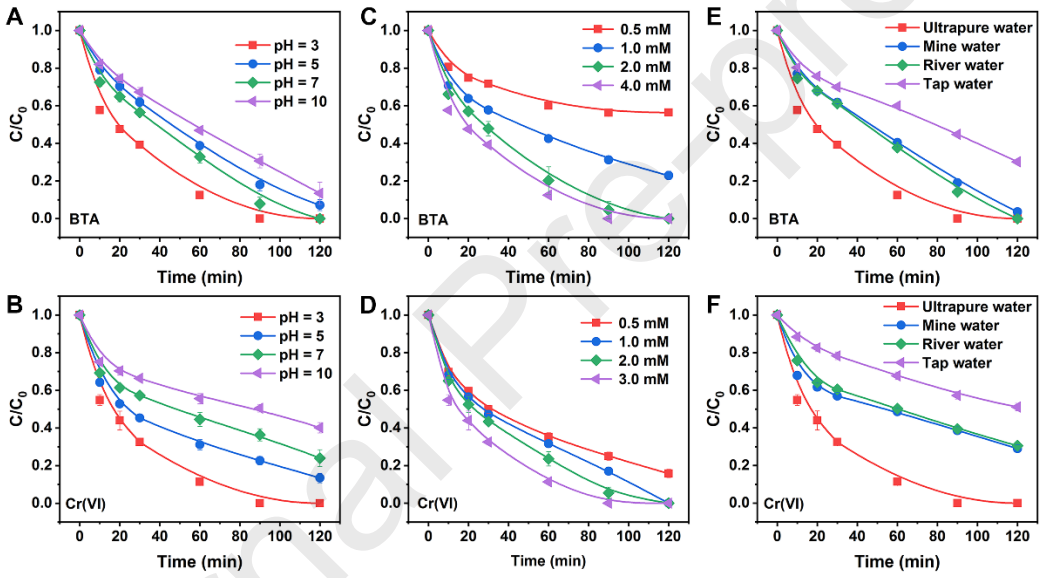

Figure 9. The impacts of the initial solution pH on BTA degradation and Cr(VI) reduction (A and B), PDS concentration (C and D) and water matrix (E and F). Reaction conditions: $[BTA]_0$ = 20 mg/L, $[Cr(VI)]_0$ = 20 mg/L, $[PDS]_0$ = 3 mM, $[CS]_0$ = 10 g/L, $[WS_2]_0$ = 4 g/L, $pH_{initial}$ = 3.0.

3.9. Stability and Reusability

As a final part of this study, the stability and reusability of the CS and WS_2 were evaluated. The characteristic peaks and mineral speciation in XRD patterns of the CS

651 and WS_2 before and after reaction show no visible changes in any of these components
652 after the reaction (Figure 1A). These results are not surprising because CS has a high
653 chemical stability due to the spinel structure of fayalite. SEM images of used CS and
654 WS_2 also show that their microstructures are consistent with those of fresh CS and WS_2
655 (Figure 1B). Obviously, both the CS and WS_2 have high stability in the treatment of
656 sewage. The recycling behavior of a CS/WS_2 mixture was evaluated in a semi-
657 continuous batch cycle experiment [34]. Five continuous cycles were conducted, and
658 each time fresh micro volumes of concentrated BTA and Cr(VI) solutions were added
659 to the system. The results in Figure S32 show that both, the removal efficiency of BTA
660 and Cr(VI) remained 100 % throughout all five cycles. These results indicated a high
661 remediation capacity of the CS/WS_2 mixture in the treatment of the combined pollution
662 in wastewater.

663 **4. Conclusions**

664 In this study, a copper slag mediated persulfate Fenton system was constructed, in
665 which WS_2 served as a co-catalyst. The applicability of this system in simultaneous
666 elimination of BTA and Cr(VI) was investigated. Fayalite was identified as the main
667 mineral component of the CS. The CS was able to release iron ions continuously for
668 AOPs, while WS_2 served as a co-catalyst in acceleration of the rate-limiting step of the
669 Fe^{3+}/Fe^{2+} conversion and in prevention of Fe^{3+} precipitation. In this process, Fe^{3+}/Fe^{2+}
670 conversion primarily occurred on the surface of WS_2, whereas decomposition of PDS
671 and degradation of BTA mainly occurred through homogeneous Fenton reactions. The

672 reactive oxygen species detection experiments showed that Fe(IV) was the main ROS,
673 followed by hydroxyl radicals and sulfate radicals. The detailed kinetics calculation
674 indicated that Fe(IV) was responsible for 63.4 % of the degradation of BTA, while
675 hydroxyl radicals and sulfate radicals accounted for 27.7 % and 8.9 % of BTA
676 degradation, respectively. The Fe^{3+}/Fe^{2+} cycle accelerated by WS_2 had a crucial role in
677 the reduction of Cr(VI). Similarly to the degradation of BTA, the reduction of Cr(VI)
678 occurred mainly through the homogeneous reactions. Dissolved Fe^{2+} had the main role
679 in the reduction of Cr(VI). Considering its low cost and good performance in a removal
680 of the organic pollutant and the heavy metal, the CS/WS_2/PDS system is considered to
681 have a good potential for the treatment of mine pollution.

682 **Acknowledgement**

683 This work has been supported partly by grants received from the National Science
684 Foundation of China (41720104007), Major National R & D Projects for Chinese
685 Ministry of Science and Technology (2019YFC1803500) as well as by the 111 Project
686 (B21017). This work also has been supported partly by 2021 Graduate Innovation Fund
687 Project of China University of Geosciences, Beijing (ZD2021YC045). This research
688 was also partially supported by the Ministry of Education, Science and Technological
689 Development of the Republic of Serbia (Grant No. 451-03-68/2022-14/200026) and by
690 the International Joint Scientific and Technical Collaboration between the People's
691 Republic of China and the Republic of Serbia as part of the Project Number 4-18.

692

References

[1] Y. Zhang, F. Wang, K.A. Hudson-Edwards, R. Blake, F. Zhao, Z. Yuan, W. Gao, Characterization of Mining-Related Aromatic Contaminants in Active and Abandoned Metal(loid) Tailings Ponds, Environ. Sci. Technol., 54 (2020) 15097-15107.https://doi.org/10.1021/acs.est.0c03368.

[2] M. Li, H. Zhong, Z. He, L. Hu, W. Sun, P. Loganathan, D. Xiong, Degradation of various thiol collectors in simulated and real mineral processing wastewater of sulfide ore in heterogeneous modified manganese slag/PMS system, Chem. Eng. J., 413 (2021).https://doi.org/10.1016/j.cej.2020.127478.

[3] H. Zhong, L. Deng, D. Luo, X. Ma, S. Wang, Preparing amide carboxylic acid compound useful as collector in mineral flotation, comprises subjecting organic carboxylic acid and amino acid compound to grinding reaction in presence of coupling reagent, China, 2019.

[4] A. Arakatsu, H. Nakazawa, H. Naruse, Flotation processes for ores contg. copper oxide, 1977.

[5] Y.T. Zhang, C. Liu, B.B. Xu, F. Qi, W. Chu, Degradation of benzotriazole by a novel Fenton-like reaction with mesoporous Cu/MnO2: Combination of adsorption and catalysis oxidation, Applied Catalysis B-Environmental, 199 (2016) 447-457.https://doi.org/10.1016/j.apcatb.2016.06.003.

[6] L. Wu, S. Suchana, R. Flick, S. Kümmel, H. Richnow, E. Passeport, Carbon, hydrogen and nitrogen stable isotope fractionation allow characterizing the reaction mechanisms of 1H-benzotriazole aqueous phototransformation, Water Res., 203 (2021) 117519.https://doi.org/10.1016/j.watres.2021.117519.

[7] A.A. Mamyrbaev, T.A. Dzharkenov, Z.A. Imangazina, U.A. Satybaldieva, Mutagenic and carcinogenic actions of chromium and its compounds, Environ. Health Prevent. Med., 20 (2015) 159-167.https://doi.org/10.1007/s12199-015-0458-2.

[8] A.D. Bokare, W. Choi, Advanced Oxidation Process Based on the Cr(III)/Cr(VI) Redox Cycle, Environ. Sci. Technol., 45 (2011) 9332-9338.https://doi.org/10.1021/es2021704.

[9] C. Kim, J.-Y. Ahn, T.Y. Kim, W.S. Shin, I. Hwang, Activation of Persulfate by Nanosized Zero-Valent Iron (NZVI): Mechanisms and Transformation Products of NZVI, Environ. Sci. Technol., 52 (2018) 3625-3633.https://doi.org/10.1021/acs.est.7b05847.

[10] P. Avetta, A. Pensato, M. Minella, M. Malandrino, V. Maurino, C. Minero, K. Hanna, D. Vione, Activation of Persulfate by Irradiated Magnetite: Implications for the Degradation of Phenol under Heterogeneous Photo-Fenton-Like Conditions, Environ. Sci. Technol., 49 (2015) 1043-1050.https://doi.org/10.1021/es503741d.

[11] T. Li, Z. Zhao, Q. Wang, P. Xie, J. Ma, Strongly enhanced Fenton degradation of organic pollutants by cysteine: An aliphatic amino acid accelerator outweighs hydroquinone analogues, Water Res., 105 (2016) 479-486.https://doi.org/10.1016/j.watres.2016.09.019.

[12] G. Sekaran, S. Karthikeyan, C. Evvie, R. Boopathy, P. Maharaja, Oxidation of refractory organics by heterogeneous Fenton to reduce organic load in tannery wastewater, Clean Technol. Environ. Policy, 15 (2013) 245-253.https://doi.org/10.1007/s10098-012-0502-5.
[13] S. Zhang, T. Hedtke, Q. Zhu, M. Sun, S. Weon, Y. Zhao, E. Stavitski, M. Elimelech, J.-H. Kim, Membrane-Confined Iron Oxychloride Nanocatalysts for Highly Efficient Heterogeneous Fenton Water Treatment, Environ. Sci. Technol., (2021).https://doi.org/10.1021/acs.est.1c01391.
[14] Y.P. Zhu, R.L. Zhu, Y.F. Xi, J.X. Zhu, G.Q. Zhu, H.P. He, Strategies for enhancing the heterogeneous Fenton catalytic reactivity: A review, Applied Catalysis B-Environmental, 255 (2019).https://doi.org/10.1016/j.apcatb.2019.05.041.
[15] R. Sharma, R.A. Khan, Sustainable use of copper slag in self compacting concrete containing supplementary cementitious materials, Journal of Cleaner Production, 151 (2017) 179-192.https://doi.org/10.1016/j.jclepro.2017.03.031.
[16] U. Erdenebold, H.M. Choi, J.P. Wang, Recovery of pig iron from copper smelting slag by reduction smelting, Arch. Metall. Mater., 63 (2018) 1793-1798.https://doi.org/10.24425/amm.2018.125106.
[17] X. Hou, X. Huang, F. Jia, Z. Ai, J. Zhao, L. Zhang, Hydroxylamine Promoted Goethite Surface Fenton Degradation of Organic Pollutants, Environ. Sci. Technol., 51 (2017) 5118-5126.https://doi.org/10.1021/acs.est.6b05906.
[18] J. Zou, J. Ma, L. Chen, X. Li, Y. Guan, P. Xie, C. Pan, Rapid Acceleration of Ferrous Iron/Peroxymonosulfate Oxidation of Organic Pollutants by Promoting Fe(III)/Fe(II) Cycle with Hydroxylamine, Environ. Sci. Technol., 47 (2013) 11685-11691.https://doi.org/10.1021/es4019145.
[19] Z. Yang, C. Shan, B. Pan, J.J. Pignatello, The Fenton Reaction in Water Assisted by Picolinic Acid: Accelerated Iron Cycling and Co-generation of a Selective Fe-Based Oxidant, Environ. Sci. Technol., 55 (2021) 8299-8308.https://doi.org/10.1021/acs.est.1c00230.
[20] G. Subramanian, G. Madras, Introducing saccharic acid as an efficient iron chelate to enhance photo-Fenton degradation of organic contaminants, Water Res., 104 (2016) 168-177.https://doi.org/10.1016/j.watres.2016.07.070.
[21] H. Sun, G. Xie, D. He, L. Zhang, Ascorbic acid promoted magnetite Fenton degradation of alachlor: Mechanistic insights and kinetic modeling, Applied Catalysis B-Environmental, 267 (2020).https://doi.org/10.1016/j.apcatb.2019.118383.
[22] T. Pan, Y. Wang, X. Yang, X.-f. Huang, R.-l. Qiu, Gallic acid accelerated BDE47 degradation in PMS/Fe(III) system: Oxidation intermediates autocatalyzed redox cycling of iron, Chem. Eng. J., 384 (2020).https://doi.org/10.1016/j.cej.2019.123248.
[23] Y. Li, Y. Wu, W. Dong, Trace catechin enhanced degradation of organic pollutants with activated peroxymonosulfate: Comprehensive identification of working oxidizing species, Chem. Eng. J., 429 (2022).https://doi.org/10.1016/j.cej.2021.132408.
[24] M. Xing, W. Xu, C. Dong, Y. Bai, J. Zeng, Y. Zhou, J. Zhang, Y. Yin, Metal Sulfides as

774 Excellent Co-catalysts for H2O2 Decomposition in Advanced Oxidation Processes,
775 Chem, 4 (2018) 1359-1372.https://doi.org/10.1016/j.chempr.2018.03.002.
776 [25] C. Dong, J. Ji, B. Shen, M. Xing, J. Zhang, Enhancement of H2O2 Decomposition by
777 the Co-catalytic Effect of WS2 on the Fenton Reaction for the Synchronous Reduction
778 of Cr(VI) and Remediation of Phenol, Environ. Sci. Technol., 52 (2018) 11297-
779 11308.https://doi.org/10.1021/acs.est.8b02403.
780 [26] Y. Zhou, L. Zhou, Y.B. Zhou, M.Y. Xing, J.L. Zhang, Z-scheme photo-Fenton system
781 for efficiency synchronous oxidation of organic contaminants and reduction of metal
782 ions, Applied Catalysis B-Environmental, 279
783 (2020).https://doi.org/10.1016/j.apcatb.2020.119365.
784 [27] X.H. Xie, R. Wang, X.X. Zhang, Y.R. Ren, T. Du, Y.S. Ni, H.L. Yan, L. Zhang, J. Sun,
785 W.T. Zhang, J.L. Wang, A photothermal and self-induced Fenton dual-modal
786 antibacterial platform for synergistic enhanced bacterial elimination, Applied Catalysis
787 B-Environmental, 295 (2021).https://doi.org/10.1016/j.apcatb.2021.120315.
788 [28] M. Huang, X.L. Wang, C. Liu, G.D. Fang, J. Gao, Y.J. Wang, D.M. Zhou, Mechanism
789 of metal sulfides accelerating Fe(II)/Fe(III) redox cycling to enhance pollutant
790 degradation by persulfate: Metallic active sites vs. reducing sulfur species, J. Hazard.
791 Mater., 404 (2021).https://doi.org/10.1016/j.jhazmat.2020.124175.
792 [29] J. Liang, X. Duan, X. Xu, K. Chen, Y. Zhang, L. Zhao, H. Qiu, S. Wang, X. Cao,
793 Persulfate Oxidation of Sulfamethoxazole by Magnetic Iron-Char Composites via
794 Nonradical Pathways: Fe(IV) Versus Surface-Mediated Electron Transfer, Environ. Sci.
795 Technol., 55 (2021) 10077-10086.https://doi.org/10.1021/acs.est.1c01618.
796 [30] H.Y. Dong, Y. Li, S.C. Wang, W.F. Liu, G.M. Zhou, Y.F. Xie, X.H. Guan, Both Fe(IV)
797 and Radicals Are Active Oxidants in the Fe(II)/Peroxydisulfate Process, Environmental
798 Science & Technology Letters, 7 (2020) 219-
799 224.https://doi.org/10.1021/acs.estlett.0c00025.
800 [31] Q. Yi, J. Ji, B. Shen, C. Dong, J. Liu, J. Zhang, M. Xing, Singlet Oxygen Triggered by
801 Superoxide Radicals in a Molybdenum Cocatalytic Fenton Reaction with Enhanced
802 REDOX Activity in the Environment, Environ. Sci. Technol., 53 (2019) 9725-
803 9733.https://doi.org/10.1021/acs.est.9b01676.
804 [32] M. Luo, H. Zhou, P. Zhou, L. Lai, W. Liu, Z. Ao, G. Yao, H. Zhang, B. Lai, Insights into
805 the role of in-situ and ex-situ hydrogen peroxide for enhanced ferrate(VI) towards
806 oxidation of organic contaminants, Water Res., 203
807 (2021).https://doi.org/10.1016/j.watres.2021.117548.
808 [33] Y. Yin, R.L. Lv, W.M. Zhang, J.H. Lu, Y. Ren, X.Y. Li, L. Lv, M. Hua, B.C. Pan, Exploring
809 mechanisms of different active species formation in heterogeneous Fenton systems
810 by regulating iron chemical environment, Applied Catalysis B-Environmental, 295
811 (2021).https://doi.org/10.1016/j.apcatb.2021.120282.
812 [34] M. Ioffe, S. Kundu, N. Perez-Lapid, A. Radian, Heterogeneous Fenton catalyst
813 based on clay decorated with nano-sized amorphous iron oxides prevents oxidant
814 scavenging through surface complexation, Chem. Eng. J., 433 (2022)

134609.https://doi.org/https://doi.org/10.1016/j.cej.2022.134609.
[35] N.M. Stover, Diphenylcarbazide as a test for chromium, J. Am. Chem. Soc., 50 (1928) 2363-2366.https://doi.org/10.1021/ja01396a007.
[36] C. Liang, C.-F. Huang, N. Mohanty, R.M. Kurakalva, A rapid spectrophotometric determination of persulfate anion in ISCO, Chemosphere, 73 (2008) 1540-1543.https://doi.org/10.1016/j.chemosphere.2008.08.043.
[37] P. Sarfo, G. Wyss, G. Ma, A. Das, C. Young, Carbothermal reduction of copper smelter slag for recycling into pig iron and glass, Miner. Eng., 107 (2017) 8-19.https://doi.org/10.1016/j.mineng.2017.02.006.
[38] Z. Guo, J. Pan, D. Zhu, Y. Congcong, Mechanism of composite additive in promoting reduction of copper slag to produce direct reduction iron for weathering resistant steel, Powder Technol., 329 (2018) 55-64.https://doi.org/10.1016/j.powtec.2018.01.063.
[39] G.P. Anipsitakis, D.D. Dionysiou, Degradation of organic contaminants in water with sulfate radicals generated by the conjunction of peroxymonosulfate with cobalt, Environ. Sci. Technol., 37 (2003) 4790-4797.https://doi.org/10.1021/es0263792.
[40] C. Zhu, G. Fang, D.D. Dionysiou, C. Liu, J. Gao, W. Qin, D. Zhou, Efficient transformation of DDTs with persulfate activation by zero-valent iron nanoparticles: A mechanistic study, J. Hazard. Mater., 316 (2016) 232-241.https://doi.org/10.1016/j.jhazmat.2016.05.040.
[41] O. Pestovsky, A. Bakac, Reactivity of aqueous Fe(IV) in hydride and hydrogen atom transfer reactions, J. Am. Chem. Soc., 126 (2004) 13757-13764.https://doi.org/10.1021/ja0457112.
[42] S. Zhu, X. Li, J. Kang, X. Duan, S. Wang, Persulfate Activation on Crystallographic Manganese Oxides: Mechanism of Singlet Oxygen Evolution for Nonradical Selective Degradation of Aqueous Contaminants, Environ. Sci. Technol., 53 (2019) 307-315.https://doi.org/10.1021/acs.est.8b04669.
[43] R. Yin, W. Guo, H. Wang, J. Du, Q. Wu, J.-S. Chang, N. Ren, Singlet oxygen-dominated peroxydisulfate activation by sludge-derived biochar for sulfamethoxazole degradation through a nonradical oxidation pathway: Performance and mechanism, Chem. Eng. J., 357 (2019) 589-599.https://doi.org/10.1016/j.cej.2018.09.184.
[44] X. Cheng, H.G. Guo, Y.L. Zhang, G.V. Korshin, B. Yang, Insights into the mechanism of nonradical reactions of persulfate activated by carbon nanotubes: Activation performance and structure-function relationship, Water Res., 157 (2019) 406-414.https://doi.org/10.1016/j.watres.2019.03.096.
[45] Y. Bu, H. Li, W. Yu, Y. Pan, L. Li, Y. Wang, L. Pu, J. Ding, G. Gao, B. Pan, Peroxydisulfate Activation and Singlet Oxygen Generation by Oxygen Vacancy for Degradation of Contaminants, Environ. Sci. Technol., 55 (2021) 2110-2120.https://doi.org/10.1021/acs.est.0c07274.
[46] E.D. Kerver, I.M.C. Vogels, K.S. Bosch, H. VreelingSindelarova, R.J.M. VandenMunckhof, W.M. Frederiks, In situ detection of spontaneous superoxide anion

and singlet oxygen production by mitochondria in rat liver and small intestine, Histochem. J., 29 (1997) 229-237.https://doi.org/10.1023/a:1026453926517.
[47] S. Bashir, M. Shaaban, Q. Hussain, S. Mehmood, J. Zhu, Q. Fu, O. Aziz, H. Hu, Influence of organic and inorganic passivators on Cd and Pb stabilization and microbial biomass in a contaminated paddy soil, J. Soils Sed., 18 (2018) 2948-2959.https://doi.org/10.1007/s11368-018-1981-8.
[48] J. Kim, H. Lee, J.-Y. Lee, K.-H. Park, W. Kim, J.H. Lee, H.-J. Kang, S.W. Hong, H.-J. Park, S. Lee, J.-H. Lee, H.-D. Park, J.Y. Kim, Y.W. Jeong, J. Lee, Photosensitized Production of Singlet Oxygen via C-60 Fullerene Covalently Attached to Functionalized Silica-coated Stainless-Steel Mesh: Remote Bacterial and Viral Inactivation, Applied Catalysis B-Environmental, 270 (2020).https://doi.org/10.1016/j.apcatb.2020.118862.
[49] C. Guan, J. Jiang, S. Pang, C. Luo, J. Ma, Y. Zhou, Y. Yang, Oxidation Kinetics of Bromophenols by Nonradical Activation of Peroxydisulfate in the Presence of Carbon Nanotube and Formation of Brominated Polymeric Products, Environ. Sci. Technol., 51 (2017) 10718-10728.https://doi.org/10.1021/acs.est.7b02271.
[50] E.-T. Yun, J.H. Lee, J. Kim, H.-D. Park, J. Lee, Identifying the Nonradical Mechanism in the Peroxymonosulfate Activation Process: Singlet Oxygenation Versus Mediated Electron Transfer, Environ. Sci. Technol., 52 (2018) 7032-7042.https://doi.org/10.1021/acs.est.8b00959.
[51] X. Cheng, H. Guo, Y. Zhang, X. Wu, Y. Liu, Non-photochemical production of singlet oxygen via activation of persulfate by carbon nanotubes, Water Res., 113 (2017) 80-88.https://doi.org/10.1016/j.watres.2017.02.016.
[52] Y. Zong, Y. Shao, Y. Zeng, B. Shao, L. Xu, Z. Zhao, W. Liu, D. Wu, Enhanced Oxidation of Organic Contaminants by Iron(II)-Activated Periodate: The Significance of High-Valent Iron-Oxo Species, Environ. Sci. Technol., 55 (2021) 7634-7642.https://doi.org/10.1021/acs.est.1c00375.
[53] R. Luo, M. Li, C. Wang, M. Zhang, M.A. Nasir Khan, X. Sun, J. Shen, W. Han, L. Wang, J. Li, Singlet oxygen-dominated non-radical oxidation process for efficient degradation of bisphenol A under high salinity condition, Water Res., 148 (2019) 416-424.https://doi.org/10.1016/j.watres.2018.10.087.
[54] M.J. Burkitt, S. Ying Tsang, S. Ching Tam, I. Bremner, Generation of 5,5-Dimethyl-1-pyrrolineN-Oxide hydroxyl and scavenger radical adducts from copper/H_2O_2 mixtures: Effects of metal Ion chelation and the search for high-valent metal–oxygen intermediates, Arch. Biochem. Biophys., 323 (1995) 63-70.https://doi.org/10.1006/abbi.1995.0010.
[55] S.K. Han, T.-M. Hwang, Y. Yoon, J.-W. Kang, Evidence of singlet oxygen and hydroxyl radical formation in aqueous goethite suspension using spin-trapping electron paramagnetic resonance (EPR), Chemosphere, 84 (2011) 1095-1101.https://doi.org/10.1016/j.chemosphere.2011.04.051.
[56] G. Nardi, I. Manet, S. Monti, M.A. Miranda, V. Lhiaubet-Vallet, Scope and limitations of the TEMPO/EPR method for singlet oxygen detection: the misleading

role of electron transfer, Free Radical Biol. Med., 77 (2014) 64-70.https://doi.org/10.1016/j.freeradbiomed.2014.08.020.
[57] S. Enami, Y. Sakamoto, A.J. Colussi, Fenton chemistry at aqueous interfaces, Proc. Natl. Acad. Sci. U.S.A., 111 (2014) 623-628.https://doi.org/10.1073/pnas.1314885111.
[58] S.Y. Pang, J. Jiang, J. Ma, Oxidation of Sulfoxides and Arsenic(III) in Corrosion of Nanoscale Zero Valent Iron by Oxygen: Evidence against Ferryl Ions (Fe(IV)) as Active Intermediates in Fenton Reaction, Environ. Sci. Technol., 45 (2011) 307-312.https://doi.org/10.1021/es102401d.
[59] L. Peng, X.G. Duan, Y.N. Shang, B.Y. Gao, X. Xu, Engineered carbon supported single iron atom sites and iron clusters from Fe-rich Enteromorpha for Fenton-like reactions via nonradical pathways, Applied Catalysis B-Environmental, 287 (2021).https://doi.org/10.1016/j.apcatb.2021.119963.
[60] Z. Wang, J. Jiang, S. Pang, Y. Zhou, C. Guan, Y. Gao, J. Li, Y. Yang, W. Qu, C. Jiang, Is Sulfate Radical Really Generated from Peroxydisulfate Activated by Iron(II) for Environmental Decontamination?, Environ. Sci. Technol., 52 (2018) 11276-11284.https://doi.org/10.1021/acs.est.8b02266.
[61] O. Pestovsky, A. Bakac, Aqueous ferryl(IV) ion: Kinetics of oxygen atom transfer to substrates and oxo exchange with solvent water, Inorg. Chem., 45 (2006) 814-820.https://doi.org/10.1021/ic051868z.
[62] H. Bataineh, O. Pestovsky, A. Bakac, pH-induced mechanistic changeover from hydroxyl radicals to iron(IV) in the Fenton reaction, Chemical Science, 3 (2012) 1594-1599.https://doi.org/10.1039/c2sc20099f.
[63] M. Huang, X. Wang, C. Liu, G. Fang, J. Gao, Y. Wang, D. Zhou, Mechanism of metal sulfides accelerating Fe(II)/Fe(III) redox cycling to enhance pollutant degradation by persulfate: Metallic active sites vs. reducing sulfur species, J. Hazard. Mater., 404 (2021) 124175.https://doi.org/10.1016/j.jhazmat.2020.124175.
[64] Y. Zhou, X. Wang, C. Zhu, D.D. Dionysiou, G. Zhao, G. Fang, D. Zhou, New insight into the mechanism of peroxymonosulfate activation by sulfur-containing minerals: Role of sulfur conversion in sulfate radical generation, Water Res., 142 (2018) 208-216.https://doi.org/10.1016/j.watres.2018.06.002.
[65] P. He, J. Zhu, Y. Chen, F. Chen, M. Gan, Pyrite-activated persulfate for simultaneous 2,4-DCP oxidation and Cr(VI) reduction, Chem. Eng. J., 406 (2020) 126758.
[66] A.D. Bokare, W. Choi, Chromate-Induced Activation of Hydrogen Peroxide for Oxidative Degradation of Aqueous Organic Pollutants, Environ. Sci. Technol., 44 (2010) 7232-7237.https://doi.org/10.1021/es903930h.

Highlights

- Solid waste CS was used as an initiator of the AOPs
- Oxidation of BTA and reduction of Cr(VI) were realized simultaneously
- WS_2 accelerated conversion of Fe(III) to Fe(II) on the surface of WS_2
- Dissolved Fe^{2+} played key roles in oxidation of BTA and reduction of Cr(VI)
- Fe(IV) was primary ROS responsible for the degradation of BTA